Aeolian Research 29 (2017) 12–22

Contents lists available at ScienceDirect

Aeolian Research

journal homepage: www.elsevier.com/locate/aeolia

Signal-adapted tomography as a tool for dust devil detection

C. Aguirre[a], G. Franzese[b,c], F. Esposito[b], Luis Vázquez[d], Raquel Caro-Carretero[e,*], Rui Vilela-Mendes[f], María Ramírez-Nicolás[d], F. Cozzolino[b], C.I. Popa[b]

[a] Universidad Autónoma de Madrid, Escuela Politécnica Superior, Calle Francisco Tomás y Valiente 11, 28260 Madrid, Spain
[b] INAF – Osservatorio Astronomico di Capodimonte, Salita Moiariello 16, 80131 Napoli, Italy
[c] Department of Physics "E. Pacini", University of Naples "Federico II", Via Cinthia, I-80126 Napoli, Italy
[d] Universidad Complutense de Madrid, Facultad de Informática, Calle Profesor José García Santesmases 9, 28040 Madrid, Spain
[e] Universidad Pontificia Comillas de Madrid, Escuela Técnica Superior de Ingeniería – ICAI, Calle Alberto Aguilera 25, 28015 Madrid, Spain
[f] Centro de Matemática e Aplicações Fundamentais, University of Lisbon C6, Campo Grande, 1749-016 Lisboa, Portugal

ARTICLE INFO

Keywords:
Mars
Dust devils
Tomography technique
Meteorology
North-Western Sahara

ABSTRACT

Dust devils are important phenomena to take into account to understand the global dust circulation of a planet. On Earth, their contribution to the injection of dust into the atmosphere seems to be secondary. Elsewhere, there are many indications that the dust devil's role on other planets, in particular on Mars, could be fundamental, impacting the global climate. The ability to identify and study these vortices from the acquired meteorological measurements assumes a great importance for planetary science.

Here we present a new methodology to identify dust devils from the pressure time series testing the method on the data acquired during a 2013 field campaign performed in the Tafilalt region (Morocco) of the North-Western Sahara Desert. Although the analysis of pressure is usually studied in the time domain, we prefer here to follow a different approach and perform the analysis in a time signal-adapted domain, the relation between the two being a bilinear transformation, i.e. a tomogram. The tomographic technique has already been successfully applied in other research fields like those of plasma reflectometry or the neuronal signatures. Here we show its effectiveness also in the dust devils detection. To test our results, we compare the tomography with a phase picker time domain analysis. We show the level of agreement between the two methodologies and the advantages and disadvantages of the tomographic approach.

1. Introduction

Dust devils are dust loaded convective vortices, with diameters of a few meters and heights of an order of magnitude larger. Their formation is favoured in conditions of strong insolation, low humidity environment, lack of vegetation and buildings or other high obstacles and gently sloping topography (Balme and Greeley, 2006). For these reasons, they are often observed in terrestrial deserts and are also very common on the surface of Mars.

Martian and terrestrial dust devils have a common formation mechanism and similar dynamics (Ringrose et al., 2003), but the Martian dust devils can be an order of magnitude larger than the terrestrial ones (Fenton et al., 2016).

Dust devils are one of the most efficient aeolian mechanisms able to lift material from the surface and inject dust into the atmosphere, through the combined effect of the vertical wind, saltation process and pressure-gradient force (Balme et al., 2003; Klose et al., 2016).

The relative importance of the three mechanisms is still unclear, but, their sum makes the dust devil a more effective dust lifting-phenomena compared to the common atmospheric boundary layer winds (Greeley et al., 2003).

On Mars, the optimum size of the grains lifted by the boundary layer winds is around 100 μm and the value of the friction velocity threshold grows rapidly for particles smaller and bigger than this optimum size. However, the typical size of grains that compose the observed Martian haze and the local and global dust storms is in the order of about 3 μm in diameter and even smaller in some cases (Pollack et al., 1979). Due to the low Martian surface pressure, the boundary layer wind required to mobilize such small grains exceeds the speed of sound (Iversen and White, 1982) and is much faster than the typical winds observed or predicted from climate models.

The small grains are indeed not directly lifted by the wind friction.

* Corresponding author at: Mullard Space Science Laboratory, Department of Space & Climate Physics, University College London, Holmbury St Mary. Dorking, Surrey RH5 6NT, UK.
E-mail addresses: carlos.aguirre@uam.es (C. Aguirre), gabriele.franzese@na.astro.it (G. Franzese), francesca.esposito@na.astro.it (F. Esposito), lvazquez@fdi.ucm.es (L. Vázquez), rcaro@comillas.edu, ucasrcc@ucl.ac.uk (R. Caro-Carretero), rvilela.mendes@gmail.com (R. Vilela-Mendes), mariarn@gmail.com (M. Ramírez-Nicolás), fabio@na.astro.it (F. Cozzolino), ciprian.popa@na.astro.it (C.I. Popa).

http://dx.doi.org/10.1016/j.aeolia.2017.09.005
Received 7 March 2017; Received in revised form 26 September 2017; Accepted 26 September 2017
Available online 06 October 2017
1875-9637/

The first particles to be mobilized by the wind are the ones whose size is around 115 μm. Bouncing on the surface, these grains (called saltators) start a chain process called saltation. At each impact with the soil other saltators are ejected and the bump can be strong enough to mobilize even the smallest particles (Greeley, 2002). The wind regime needed to start the saltation on Mars is quite uncommon, but, once started the process can be sustained by the typical Martian winds (Almeida et al., 2008; Kok and Renno, 2009; Kok, 2010).

The wind friction and the saltation processes represent the driving lifting mechanisms during the dust storm. However, the lifting power of dust devils appears to be effective in a range of grain size much larger than the one of the wind friction (Neakrase and Greeley, 2010a,b). In addition, the vortices are a continuous source of lifted dust also outside the dust storms season. For these reasons, the dust devils have been proposed as one of the main mechanisms able to sustain the dust haze of the Martian atmosphere (Neubauer, 1966; Thomas and Gierasch, 1985, Klose et al., 2016).

The pressure gradient force is due to the low-pressure core at the centre of the dust devil. In the simplest and most common case, when the vortex has a single core, the pressure profile can be approximated by a Lorentzian function (Ellehoj et al., 2010):

$$P(t) = \frac{-\Delta P}{1 + \left(\frac{t - t_o}{1/2\Gamma}\right)^2} + B$$

where P(t) is the pressure as a function of time, ΔP is the magnitude of the pressure dip at the centre of the vortex, t_o is the time instant relative to the peak, B is the background pressure value and Γ is the full width at half maximum (FWHM) of the event. The cumulative distribution of the ΔP can be described by a power law function, the magnitude of the drop usually ranges from 0.1 to 1.5 mbar (Lorenz and Jackson, 2016).

The sand and dust grains mobilized by the vortex collide with each other and with the surface, acquiring charge by triboelectricity (Eden and Vonnegut, 1973). When the composition of the colliders is approximatively heterogeneous, the charging process is size-dependent, the smaller grains tending to acquire a charge opposite to the larger ones (Inculet et al., 2006; Duff and Lacks, 2008; Esposito et al., 2016; Harrison et al., 2016; Neakrase et al., 2016). The smaller grains are lighter and are driven upwards in the dust column by the air flow, while the larger ones stay closer to the ground producing a charge separation. The dust devil can acquire a strong electric field in this way, as firstly reported by Freier (1960), Crozier (1964, 1970). Farrell et al. (2004) has reported for terrestrial dust devils a vertical electric field over 4000 V/m. Taking into account that usually the background absolute value of the terrestrial atmospheric electric field is below 100 V/m, the electrical variation due to the passage of a dust devil is a clearly recognizable feature of the event.

As already mentioned, the role and importance of dust devils in the Martian climate is a highly studied and debated subject. The study of dusty vortices is one of the scientific questions to be pursued by the next Mars space missions, such as the ExoMars 2020 and InSight 2018 (Lorenz, 2016). Therefore, the ability to discriminate dust devils in the acquired data becomes of great importance.

Overall, the main signatures of the passage of a dust devil are (Balme and Greeley, 2006):

- a peak in wind speed,
- a change in wind direction,
- a drop in pressure,
- a peak in the electric field,
- a peak in concentration of the lifted dust and sand,
- a raise in atmospheric temperature.

Depending on the distance to the dust devil and on its magnitude, these features can be more or less evident and some of them may be totally hidden. Clearly, the simultaneous occurrence of all of them strongly indicates the passage of a dusty vortex. The detection of dust devils starts from the search for one of these features. Usually, the variation in the pressure signal is chosen as the main parameter to investigate (Murphy et al., 2016).

Methods based on the comparison between a short-term and a long-term average are used to detect the isolated drops. This approach is called “phase picker”. In dust devils the long-term average is usually in the order of ten minutes, while the short-term is in the order of ten seconds or less. When the difference between the two values exceeds a chosen threshold the event is counted as a possible dust devil. The threshold depends on the fluctuations around the long-mean value, namely, on the variability and noisiness of the signal. Subsequent check of the other physical parameters allows the elimination of non-significant events. This method is used, with some variants, both on terrestrial (e.g., Jackson and Lorenz, 2015) and on Martian (e.g., Ellehoj et al., 2010) measurements.

Here we want to propose an alternative technique based on a time-signal adapted operator analysis, instead of the direct time analysis. This technique allows us to deal with very noisy signals and it is less sensitive to the duration and magnitude of the dust devil’s signal, leading to a detection much less sensitive to the choice of arbitrary thresholds. This tool also allows to filter the signal eliminating any component that does not belong to the dust devil.

The pressure profile of the vortex has a clear shape in the time domain but has no characteristic track in the frequency domain. Therefore, we need a signal transform that takes into account transients and allows the extraction of the signal components that are related to the characteristic behaviour of the dust devils. For this purpose, we decided to adopt a bilinear transformation called tomogram, improving the technique and adapting it to the specific case of the vortices detection.

The analysed data were acquired during a field campaign performed in Morocco in 2013. The campaign was carried out in the frame of the DREAMS project, the meteorological station on board of the Schiapparelli lander of the ExoMars 2016 space mission (Esposito et al., 2017). We show the results of the application of this new methodology to the data acquired during five days of measurement. We show the results of the application of this new methodology to the data acquired during five days. We have also analysed the same days with a time-domain technique. Comparing the corresponding results obtained by the two methods, we can test the effectiveness of the tomographic technique.

2. Material and methods

2.1. Field campaign

The field campaign took place in 2013 in the Tafilalt region (Morocco) in the north-western Sahara. This area is characterized by an arid environment, it is rich in both sand and dust, and is very active from an aeolian point of view. Measurements have been performed during the dust storm season in a period between July and September at geographical coordinates 4.113°W, 31.161°N, elevation of 797 m a.s.l.

From the geological point of view, this site is a flat Quaternary lake sediment bed. The sand, silt and clay fractions of the soil have similar composition consisting of detrital shale grains, quartz and carbonates. The position near the centre of the lake made the site rich in hygroscopic and soluble minerals. For this reason, most of the soil grains are aggregated in an extended saline crust.

A fully equipped meteorological station (Fig. 1) was deployed consisting of:

- soil temperature (CS thermistor) and moisture (CS616-C) sensors,
- three 2D sonic anemometers (Gill WindSonic) placed at 0.5, 1.41, 4 m,
- one temperature and humidity sensor (Vaisala HMP155) at 4.5 m

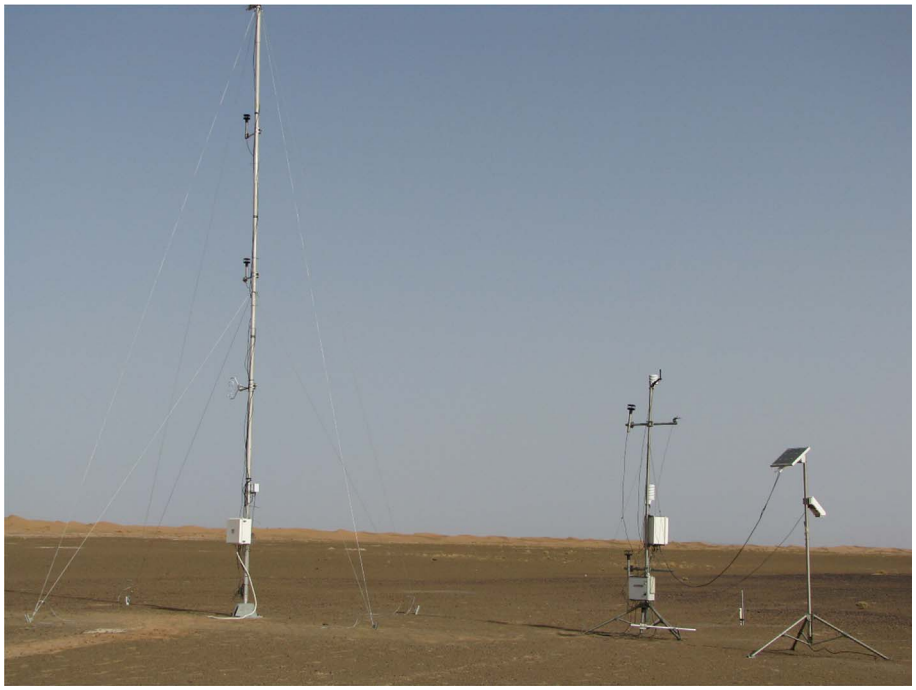

Fig. 1. Meteorological station deployed in the Moroccan desert.

and one thermometer (Campbell Sci. (CS)) placed at 2.5 m,
- pressure sensor (Vaisala Barocap PTB110) at 2 m,
- solar irradiance sensor (LI-COR LI-200 Pyranometer) at 4 m,
- atmospheric electric field sensor (CS110) faced down at 2 m.

In addition, to monitor the sand and grain motion were deployed also:

- a size-resolved airborne dust concentration sensor at 1.5 m (Grimm EDM 164-E) that analyses dust in 31 channels in the range 0.265–34 μm,
- two sand impact sensors (Sensit Inc.) for the detection of saltating sand grains,
- three sand catchers (BSNE) at different heights (12, 25 and 40 cm) for daily collection of sand in saltation.

The station was set to operate 24 h/day at a sampling rate of 1 Hz. A solar panel system powered the station. Further details on the site and on the field campaign measurements can be found in Esposito et al. (2016).

2.2. The tomographic technique

Integral transforms are useful tools for signal analysis in many fields of science, the Fourier transform (Fourier, 1988) and the Wavelet transform (Daubechies, 1990) being among the most popular of these transforms. However, the Fourier transform does not provide information on the transient behaviour of the signal, as time information is spread over the phases of the transform coefficients. Wavelet transform provides some localization but it presents problems in the interpretation of the coefficients and is not an appropriate tool for signals that do not present a multi-resolution behaviour. Localized transforms, such as the Windowed Fourier transform, allow some localization of the transform coefficients, but require a compromise in the size of the window due to the Heisenberg uncertainty principle for signals (Donoho and Stark, 1989). Shorter window sizes, allow a good localization in time but reduce the capacity of detection of low frequency components in the signal, on the other hand, longer window sizes reduce the capacity of time localization of the transform.

Bilinear transforms are frequently used to provide information in the time-frequency domain. Among these transforms, the Wigner-Ville quasi-distribution (Wigner, 1932) is the most commonly used. The Wigner-Ville quasi-distribution has the problem that spurious or even negative terms also appear in areas where there is no signal at all. The Wigner-Ville quasi-distribution can be seen as a windowed version of the Wigner-Ville distribution and presents the same problems of compromise in the size of the window as the Windowed Fourier Transform. The Wigner-Ville quasi-distribution does not guarantee the absence of spurious terms and may present a meaningless spread in the physically correct time-frequency regions.

These problems in the bilinear transforms arise from the fact that time and frequency are two noncommutative operators and therefore a joint probability distribution cannot be defined, even in the case of positive quasi probabilities, such as the Husimi-Kano function (Husimi, 1940; Kano, 1965).

Tomograms (Man'ko and Mendes, 1999) are strictly positive bilinear transforms. They are a generalization of the Radon transform to arbitrary pairs of non-commutative operators, the Radon-Wigner transform being a particular case of a tomogram. These transforms are strictly positive probability densities that provide a full characterization of the signal. A complete characterization of the tomogram transforms may be found in Man'ko et al. (2001). The transforms are obtained from the projections on the eigenstates of self-adjoint operators B obtained as a linear combination of a pair of commuting or non-commuting operators O_1 and O_2.

$$B(\mu,\nu) = \mu O_1 + \nu O_2$$

Following this method, tomograms have been built for several pairs of operators. Of special interest is the time-frequency operator:

$$B_{tf}(\mu,\nu) = \mu t + \nu\omega = \mu t + \nu(-i\frac{\partial}{\partial t})$$

Taking $\mu = \cos(\theta)$ and $\nu = \sin(\theta)$ one obtains an operator that depends on a single value $\theta \in (0, \pi/2)$ interpolating between the time and frequency operators:

$$B_{tf}(\theta) = \cos(\theta)t + \sin(\theta)\left(-i\frac{\partial}{\partial t}\right)$$

When $\theta = 0$ we are in the time domain and when $\theta = \pi/2$ we are in

the frequency domain.

The construction of the time-frequency tomogram reduces to the calculation of the generalized eigenvectors of the operator B_{tf}. For example, the projection $M_f(\theta,X)$ for a finite time signal $f(t)$ defined in an interval t_0 to $t_0 + T$ is:

$$M_f(\theta,X) = |\int_{t_0}^{t_0+T} f^*(t)\psi_{\theta,X}(t)dt|^2 = |f,\psi|^2$$

where $\psi_{\theta,X}(t)$ are the eigenfunctions of operator B_{tf}, namely

$$\psi_{\theta,X}(t) = \frac{1}{\sqrt{T}} exp\left(\frac{i\cos\theta}{2\sin\theta}t^2 + \frac{iX}{\sin\theta}t\right)$$

Time-frequency tomograms have already been used to remove noise and separate the signal components in many scientific fields. For example, in (Briolle at al., 2012) time-frequency tomograms were used for plasma reflectometry and in (Aguirre et al., 2013) neuronal signatures (i.e., characteristic time patterns in firing neurons that conform a specific message to other neurons) are detected by means of tomography.

The concept of signal component is not uniquely defined and the notion of a component depends not only on the observed signal but also on the specific features that we are interested on. A signal component might, for example, be a component with some specific signature in the time or in the frequency domain. However, signal components are not always easy to define as time or frequency signatures, and sometimes there is not a simple analytical description of the component that we are looking for. Even if a clear description is available, the component can be still hidden by noise. This makes the separation in the time domain a difficult issue. Moreover, in the frequency domain the component might not have a characteristic signature and be hidden by other components.

The dust devils pressure drop has a clear time behaviour (as mentioned in introduction). This trend, due to the atmospheric pressure variation, could be totally or partially hidden by noise. Moreover, in the frequency domain, dust devils pressure does not possess a characteristic behaviour. This fact suggests that a different kind of tomograms should be used. In this new tomogram one of the operators should be adapted to the characteristics of the component we want to separate.

A new type of signal-adapted tomogram has recently been proposed by (Aguirre and Vilela Mendes, 2014) with the detection of dust devils in mind (Gimenez-Bravo et al., 2013). The signal-adapted tomogram is a linear combination of a standard operator, such as time or frequency with an operator O that is specially tuned to the features of the component that one wants to extract:

$$B(\mu,\nu) = \mu\ t + \nu O$$

As in the time-frequency tomogram a particular set of (μ,ν) pairs can be selected by a single parameter θ, with $\mu = \cos\theta$, $\upsilon = \sin\theta$. It is possible to separate the signal components we are interested in from the noise components by looking for particular values of θ where noise or undesired components cancel or becomes small, as high concentration of energy in some coefficients of the transform means that the signal contains the component we are looking for. This has the additional advantage that we can retain information about the temporal structure of the signal. The construction of signal-adapted operators follows the same technique as used in the bi-orthogonal decomposition of signals (Aubry et al., 1991, Dente et al., 1996).

Consider a set of k N-dimensional time sequences $\{\overrightarrow{x_1},\overrightarrow{x_2},...,\overrightarrow{x_k}\}$ that are typical representations of the component one wants to detect. This set of time sequences can be represented by means of a k × N matrix U, with usually k < N:

$$U = \begin{pmatrix} x_1(1\Delta t) & x_1(2\Delta t)\cdots & x_a(N\Delta t) \\ \vdots & \ddots & x_a(N\Delta t) \\ x_k(1\Delta t) & x_k(2\Delta t)\cdots & x_{bk}(N\Delta t) \end{pmatrix}$$

We now construct the square matrix:

$$A = U^T U \in \mathcal{M}_{N\times N}$$

The diagonalization of A provides k non-zero eigenvalues $(\alpha_1,\alpha_2,...\alpha_k)$ and the corresponding k N-dimensional eigenvectors $(\Phi_1,\Phi_2,...\Phi_k)$.

Now a linear operator S can be constructed from the previous set of eigenvectors in the following way:

$$S = \sum_{i=1}^{k} \alpha_i \Phi_i \Phi_i^T \in \mathcal{M}_{N\times N}$$

To construct the time-data tomogram we build the time operator for discrete time in the following way:

$$t = \begin{pmatrix} 1\Delta t & & & \\ & 2\Delta t & & \\ & & \ddots & \\ & & & N\Delta t \end{pmatrix} \in \mathcal{M}_{N\times N}$$

and to generate the tomogram we consider a linear operator $B(\mu,\nu)$ of the form:

$$B(\mu,\nu) = \mu t + \nu S = \mu \begin{pmatrix} 1\Delta t & & & \\ & 2\Delta t & & \\ & & \ddots & \\ & & & N\Delta t \end{pmatrix} + \nu \sum_{i=1}^{k} \alpha_i \Phi_i \Phi_i^T \in \mathcal{M}_{N\times N} \quad (1)$$

As usual, parameters μ and υ are considered in the form $\mu = \cos\theta$, $\upsilon = \sin\theta$.

Now proceeding in a way like the time-frequency operator, we obtain the N eigenvectors $\{\overrightarrow{\psi}_\theta^1, \overrightarrow{\psi}_\theta^2, ..., \overrightarrow{\psi}_\theta^N\}$ of operator $B(\theta)$. Projections of the signal $\overrightarrow{X}$ on these eigenvectors are obtained by

$$c_\theta^i = \overrightarrow{X}, \overrightarrow{\psi}_\theta^i \text{ for } i = 1,2,...,N$$

These projections construct a tomogram adapted to the operator pair t, S.

Once the tomogram is constructed, the signal can be denoised or decomposed just by considering the set of values that contain a given amount of the total energy of the signal or by considering only the coefficients with an absolute value over a given threshold $c_\theta^i \geqslant \in$ with $\in$ being a fixed threshold or a function that depends on the whole set of coefficients $\{c_\theta^1, c_\theta^2, ..., c_\theta^N\}$. In this work $\in$ is taken as a fixed value multiplied by the spectrum average $\frac{1}{N}\sum_{j=1}^{N}|c_\theta^i|$, this is

$$\in = k\frac{1}{N}\sum_{j=1}^{N}|c_\theta^i|$$

If we consider only the indexes $i = i_1, i_2, ..., i_h$ for wich $c_\theta^i \geqslant \in$ we obtain a subset of h coefficients $C = \{c_\theta^{i_1}, c_\theta^{i_2}, ..., c_\theta^{i_h}\}$. Signal $\overrightarrow{x}^f$ is now reconstructed by considering only the vectors $\{\overrightarrow{\psi}_\theta^{i_1}, \overrightarrow{\psi}_\theta^{i_2}, ..., \overrightarrow{\psi}_\theta^{i_h}\}$ of the tomogram that are in subset C, this is:

$$\overrightarrow{x}^f = \sum_{j=1}^{h} c_\theta^{i_j} \overrightarrow{\psi}_\theta^{i_j}$$

2.2.1. Event detection

As dust devils produce a drop in the pressure value we have built a 277 × 1000 matrix U that contains a set of 277 typical signals of 1000 s duration, containing a drop of 15% from the baseline with durations ranging from 20 to 60 s and normalized to zero mean. With this method, the amount of drop is not significant so we have selected a drop that works well in many environments, for example this set of signals could be used in atmospheres with a lower pressure level or dust-devil like phenomena produce a higher drop in the pressure signal, as happens in Mars atmosphere. In Fig. 2 a set of several of this type of signals shifted in value for a better view is depicted.

From the Matrix U we build Matrix A and finally we build the *signal-adapted* operator S as described in the previous section. Fig. 3 is a plot of

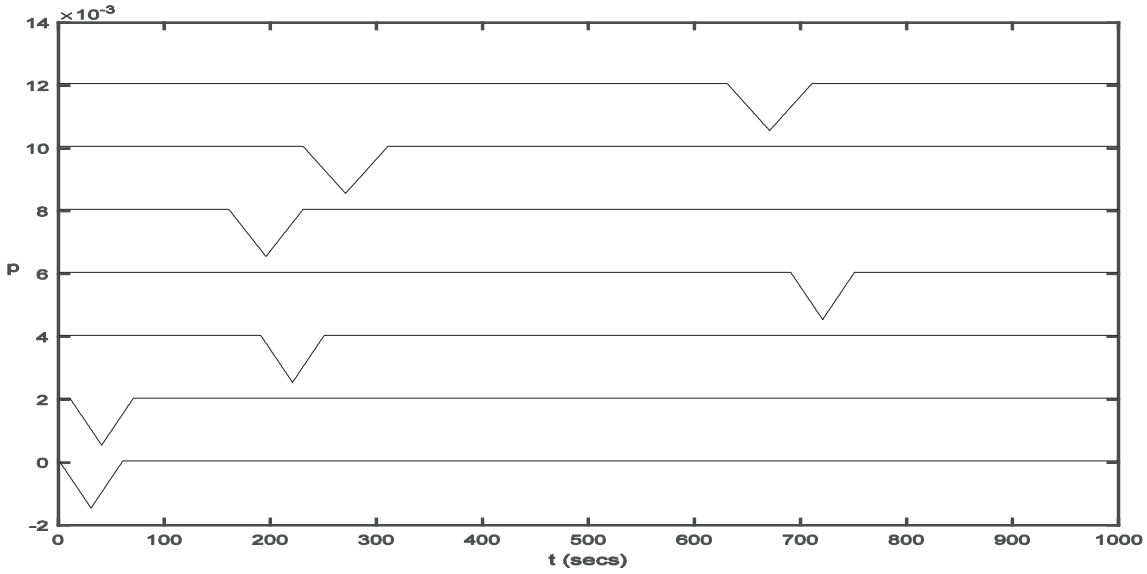

Fig. 2. Sample set of normalized to zero mean typical signals. Time is measured in seconds and p represents normalized pressure. Some signals are shifted in value for a better view.

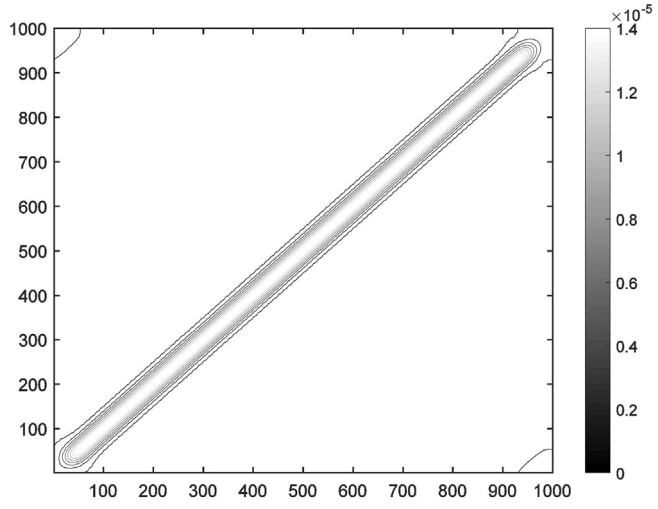

Fig. 3. The signal-adapted operator Matrix S.

the signal-adapted operator S; each point in the plot represents a value in matrix S, showing that operator is symmetric and definite positive.

Finally, we build the tomogram with the linear combination $B(\theta) = \cos(\theta)t + \sin(\theta)S$ for the values $\theta = \frac{\pi l}{40} l = 1,2...20$.

We break up our signal in 1000-s samples with a 200-s margin from the previous sample to avoid losing events close to the border. To avoid high-energy coefficients in the transform we normalize the signals to zero mean. In Fig. 4 a 1000-s sample with a possible dust devil event is depicted (observed at '2013-08-10 16:44:39').

In Fig. 5 a plot of the $B(\theta)$ -tomogram applied to the previous sample is depicted. For all values of θ there exists a clear peak close to coefficient c_{θ}^{450}.

In Fig. 6 the projection of the data for $\theta = \frac{\pi}{4}$ is depicted showing that, effectively a clear peak exists close to the coefficient $c_{\frac{\pi}{4}}^{500}$. In order to avoid border effects, the first and last coefficient of the projection are discarded, as these coefficients tend to concentrate the energy of the signal that does not correspond to dust devil events. To detect relevant events any standard filtering technique can be applied, for example, you can consider coefficients that are over a given fixed threshold or coefficients that are clearly over the average value of the transformed signal. Higher values of the coefficients correspond to clearer dust devil events.

We can now filter the signal just keeping a small set of values close to the most significant value and reconstructing the dust devil component. In Fig. 7 a reconstruction from coefficients from $c_{\frac{\pi}{4}}^{495}$ to $c_{\frac{\pi}{4}}^{505}$ is depicted. It can be observed that any component of the signal that does not behave as a dust devil is removed. To obtain the duration of the dust devil just consider the values that are different from zero, and to obtain the pressure drop just de-normalize the filtered signal.

As explained in Section 2.2, to identify the dust devil components of the signal we make use of the spectrum average, this is $\frac{1}{N}\sum_{j=1}^{N} |c_{\theta}^{j}|$, where c_{θ}^{i} are coefficients of the tomographic transform of the signal. The clearer the dust devil event is, the bigger is the corresponding coefficient or set of coefficients in the tomographic transform, so we

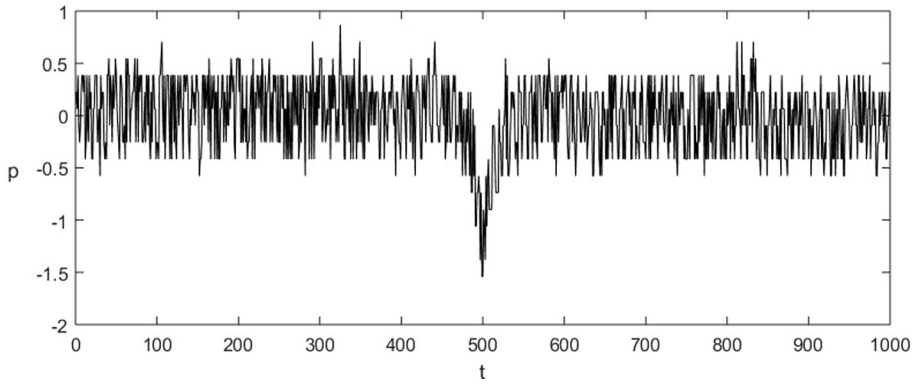

Fig. 4. Pressure data containing a possible dust devil event observed at '2013-08-10 16.7441667, 16:44:39'. Signal is normalized to zero mean to avoid high energy coefficients.

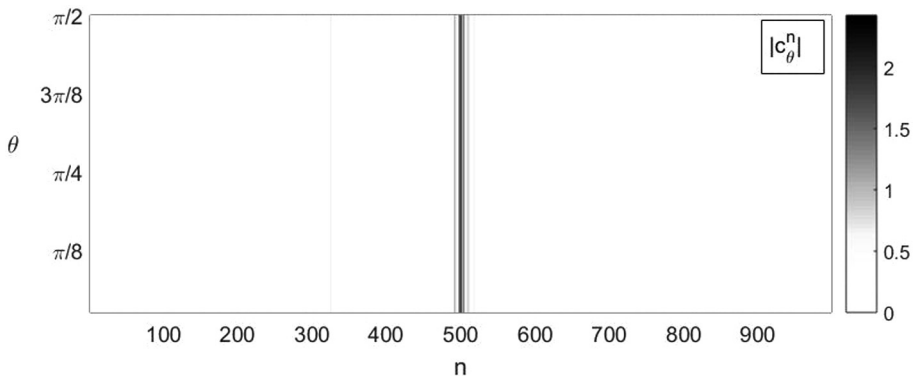

Fig. 5. Plot of the tomogram for pressure data. A clear peak is visible at coefficient c_θ^{500} for most values of θ.

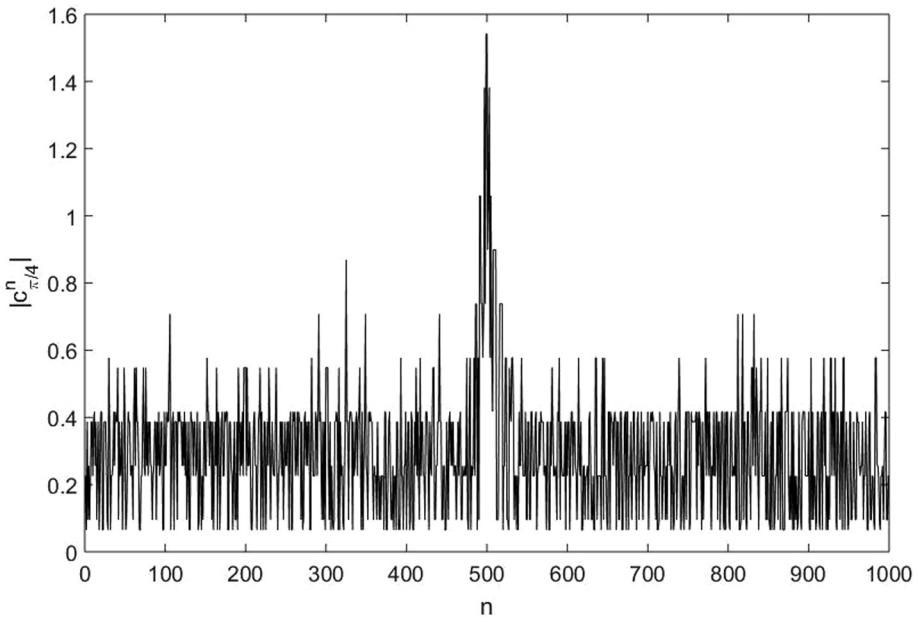

Fig. 6. Projection of the pressure data tomogram for $= \frac{\pi}{4}$.

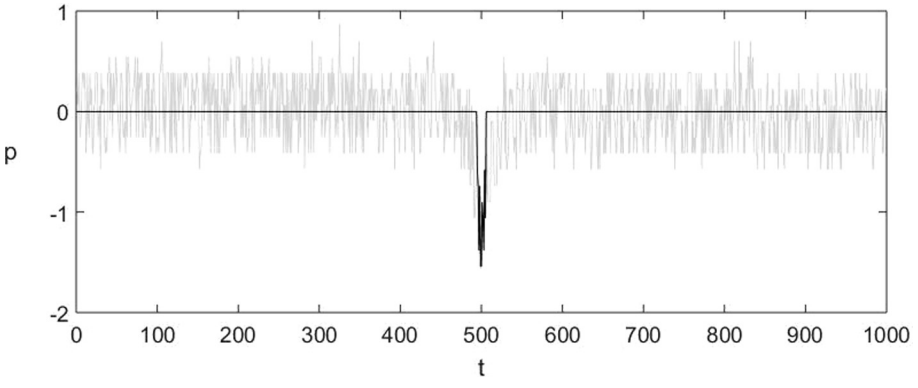

Fig. 7. Original (gray) and reconstructed (black) signal from coefficients from $c_{\frac{\pi}{4}}^{495}$ to $c_{\frac{\pi}{4}}^{505}$ of event T38 detected at '2013-08-10 16.7441667, 16:44:39'.

Table 1
Classes and main characteristics regarding the division of the events identified by the Tomography technique.

Tomography technique	
Classes	Main Characteristics
E	Transform coefficient > 6·spectrum average
D	Transform coefficient > 6,5·spectrum average
C	Transform coefficient > 7·spectrum average
B	Transform coefficient > 7.5·spectrum average
A	Transform coefficient > 8·spectrum average

classify the dust devil event depending of the relative size with the spectrum average. As can be seen in Fig. 5, the event can be clearly detected for any value of θ, and therefore we have opted for the simplest solution of taken a fixed value of $\theta = \frac{\pi}{4}$.

The detected events have been divided into classes from the least probable to the most probable depending on the relative magnitude of the transform coefficient from the spectrum average. We labelled the events with an ID that starts with T. The classification used is in Table 1.

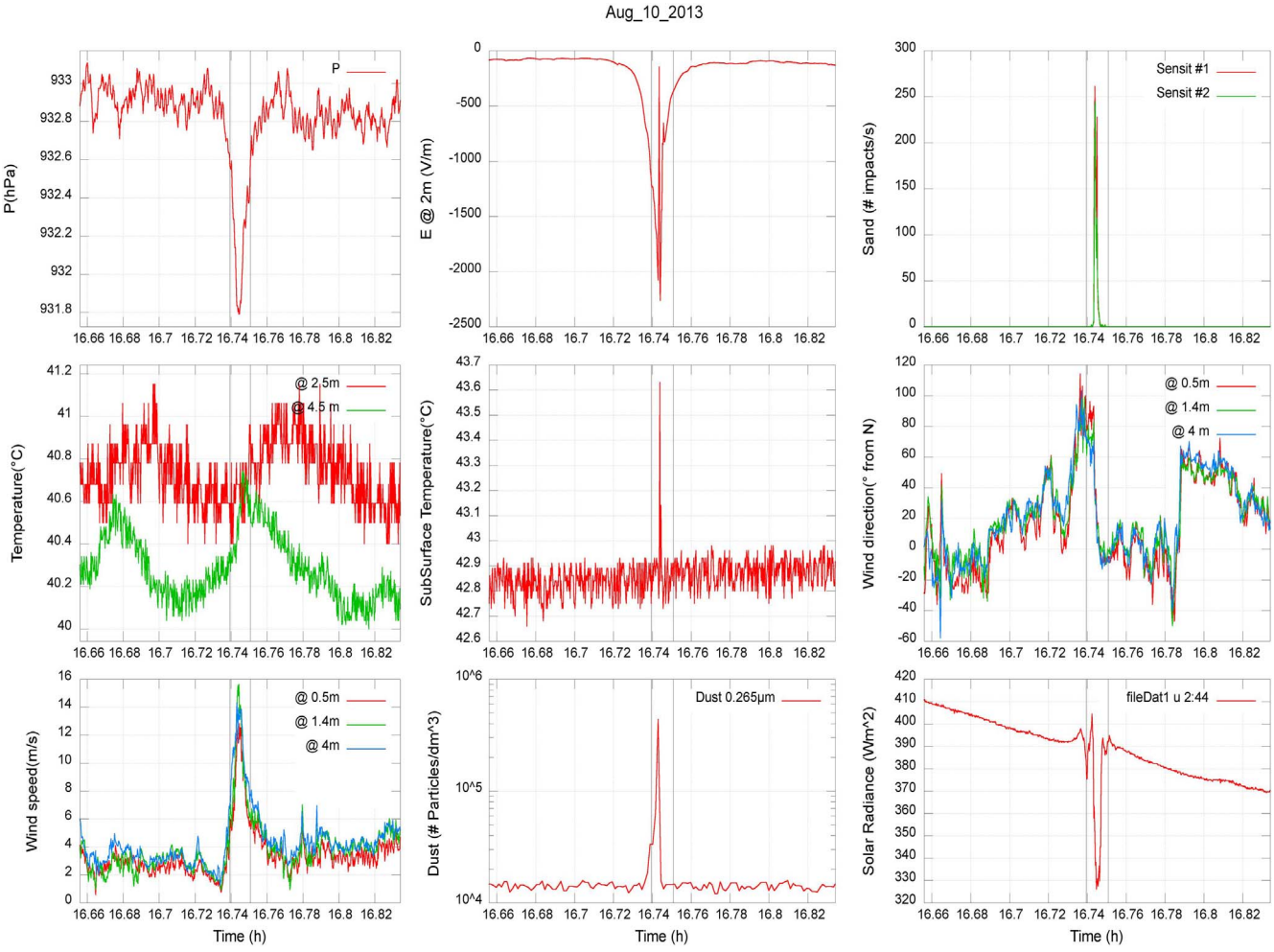

Fig. 8. A dust devil at '2013-08-10 16.7441667, 16:44:39' identified by the meteorological instruments.

Table 2
Classes and main characteristics regarding the division of the events identified by the time domain research technique performed on three parameters (pressure, wind direction and electric field).

Time domain research technique	
Classes	Main Characteristics
D	The event is a false positive, where the dust devils features are certainly not recognizable.
C	The pressure drop is barely observable and there are weak variations in electric field, wind speed and direction. The signal usually shows also features hardly compatible with a dust devil, i.e., a peculiar shape or anomalous time duration. The event probably is not a dust devil
B	The magnitude of the pressure drop is comparable with the noise level so could be partially hidden. However, the event shows a clear peak for each of the other main parameters. The event is probably a dust devil
A	The event shows a clear peak for each of the main parameters, it is clearly recognizable as a dust devil

2.3. Time domain research technique

We want to compare the results obtained by the tomography method with those obtained by the direct analysis of the time domain signal.

In order to detect the passage of a dust devil in the data we have compared a long term with a short-term mean, to determinate the fast variations in the signal. This kind of analysis, called "phase picker", is the most common for the dust devil detection and is usually performed on the atmospheric pressure time series (Lorenz and Jackson, 2016). Indeed, as we have seen (Eq. (1)), the pressure variation is a distinctive characteristic of the dust devil encounters. The passage of the vortex lasts only a few seconds in the data, so both the long-term time interval and the short one have to be as short as possible. Our choice of the long-term mean, 12 min, is similar to the one commonly used in literature (e.g. Jackson and Lorenz 2015). The standard deviation of the pressure measurements around this long term is on average of 0.3 mbar. This noise level is too high to allow a clear detection of the medium magnitude signals and it could totally cover the weaker encounters.

In order to use the standard phase picker method on the pressure time series we need to filter the noise. For this purpose, we have used a running average on a time window of 11 s. The extension of the window would lead to a further cut of the noise but also to a reduction of the drop magnitude, until the complete elimination of the dust devils signals. After the application of the filter the standard deviation around the long-term mean is on average of 0.1 mbar; we can use then our measurements taken at 1 Hz rate as the short term values.

We have developed software that analyses the filtered data, dividing the whole day in time intervals of 12 min. For each one it evaluates the median value of the atmospheric pressure. When the instantaneous pressure value and the median one differ for more than a given limit (ΔP_{lim}), the event is selected. In the following, we will refer to these detections as class T events. However, the detection of an isolated pressure drop is not enough to confirm the events as dust devil, indeed we need the simultaneous occurrence of one or more other meteorological signatures described in Section 1. For this reason, the software analyses the variations of wind direction and electric field during the

Table 3
List of the events identified with the tomography technique. The date, the initial instant, the tomogram class and the result of the manual crosscheck are reported. The results of the crosscheck are simply given in term of yes and no, except one case for which the meteorological data is not conclusive and the event is catalogued as possible. We also indicate the events recognizable as convective not dust loaded vortices.

ID	Date	ti(h)	Tomograms Class	Full parameters Crosscheck
T1	17_07_2013	4.7944445	E	No
T2	17_07_2013	4.8316667	E	No
T3	17_07_2013	4.8650000	E	No
T4	17_07_2013	5.0838889	E	No
T5	17_07_2013	5.1352778	D	No
T6	17_07_2013	5.4038889	D	No
T7	17_07_2013	5.4352778	D	No
T8	17_07_2013	7.0977778	E	No
T9	17_07_2013	9.6669445	E	Not dusty Vortex
T10	17_07_2013	14.0333333	E	No
T11	17_07_2013	15.5966666	D	Yes
T12	17_07_2013	15.8788889	D	Not dusty Vortex
T13	17_07_2013	16.0333333	D	No
T14	17_07_2013	18.9736111	A	Yes
T15	17_07_2013	19.5730556	D	No
T16	17_07_2013	20.0319444	D	No
T17	17_07_2013	20.5786111	B	No
T18	17_07_2013	20.6494444	B	Yes
T19	17_07_2013	21.5641667	A	Yes
T20	21_07_2013	8.4327778	D	No
T21	21_07_2013	12.8000000	A	Yes
T22	21_07_2013	13.3691667	B	Yes
T23	21_07_2013	14.9480556	D	No
T24	21_07_2013	15.7708333	D	No
T25	21_07_2013	18.6238889	D	No
T26	24_07_2013	8.7080555	D	No
T27	24_07_2013	9.0041667	D	Not dusty Vortex
T28	24_07_2013	9.6888889	B	Yes
T29	24_07_2013	10.9250000	B	Yes
T30	24_07_2013	11.0016667	D	Possible
T31	24_07_2013	11.5891666	D	Yes
T32	24_07_2013	16.8805556	B	Yes
T33	10_08_2013	0.0497222	E	No
T34	10_08_2013	4.8011111	E	No
T35	10_08_2013	11.9986111	D	No
T36	10_08_2013	12.2894444	D	No
T37	10_08_2013	13.9894444	D	Not dusty Vortex
T38	10_08_2013	16.7441667	A	Yes
T39	10_08_2013	17.9986111	D	No
T40	11_08_2013	1.9922222	E	No
T41	11_08_2013	3.9872222	E	No
T42	11_08_2013	5.9919444	E	No
T43	11_08_2013	9.9916667	D	Not dusty Vortex
T44	11_08_2013	11.4319444	B	Yes
T45	11_08_2013	13.0125000	C	Yes
T46	11_08_2013	13.9905556	C	No
T47	11_08_2013	19.9902778	C	No

selected events. If both these variations overcome the chosen thresholds, ΔW_{lim} and ΔE_{lim}, the event is identified as a dust devil. We have used the following values for the limits: $\Delta P_{lim} = 0.18$ mbar, $\Delta W_{lim} = 30^{\circ}$, $\Delta E_{lim} = 50$ eV. Indeed, these values give a good compromise between the possibility of detecting even the small dust devils and the ability to cut off the main part of the non-significant events. For further explanation on the method, see Franzese et al. (2017).

Fig. 8 shows how one of the detected events (the same event of Fig. 7) appears in the whole set of measured parameters.

Here we are not interested in testing the reliability of the phase picker technique, but we are looking for possible dust devils not seen by the tomographic technique. Hence we decided to classify the events after a crosscheck of every measured parameter, in order to verify if they are or not true dust devils. We have used the classes shown in Table 2, labelling the events with an ID that starts with P.

3. Results and discussion

In this section, we show the results obtained through the application of two research techniques.

Our purpose is to evaluate the reliability and effectiveness of the tomography. For this reason, we have initially crosschecked all the events identified by the tomography, through the analysis of the entire set of meteorological parameters, in order to confirm if the dust devil's signatures are recognizable or not. Then we have compared the results of the tomography with those obtained by the direct time domain research.

The tomography technique has identified 47 dust devils candidates: 12 class E, 21 class D, 3 class C, 7 class B and 4 class A events. The crosscheck of these events confirms that all the class A events are recognizable as dust devils, while all the class E ones are not. Regarding the class B events, just one seems not to be a dust devil, while, there are two other "not dust devil" events in the class C. Three of the class D events are recognizable as dust devils, 4 seem to be not a dusty convective vortex, while the remaining ones appear to be wind gusts or related to dust storms.

The complete list of the detected events and the results of the manual check are given in Table 3.

The signal-adapted tomogram used in this work was constructed for the pressure time series only. Therefore, in theory, this method has no possibility of distinguish between the dusty and the not dusty vortices. However, any of the detected "not dust loaded vortices" belong to the most probable classes A and B, they all fall in the lower classes D and E.

Fig. 9 shows the number of true dust devils in every class normalized by the number of events in the class. It is clear how the percentage of true dust devils in every class rapidly grows towards the A class and it is highly probable that the events belonging to the higher class A and B are true dust devils. This proves the affability of the tomography technique and the reliability of the chosen classification.

As said, the small values of the thresholds that we are using have the advantage of detecting even the smaller dust devils. On the other hand, this increases the number of false detections. Out of the 361 dust devils candidates, 328 are non-significant events (class D). Of the remaining 23 detections, 6 are class C, 2 are class B and 15 are class A events. We report in Table 4 only the possible dust devils (class A, B and C).

We focused on the best candidates detected by the time domain research (class A and B), comparing the results with the ones obtained by tomography. As it can be noted in Table 5, the events detected are in good agreement for all the data. There are only 4 events not detected by tomography: two class B and two class A, and they all happened during July, 17th. Overall, there is a match of 12 events over 16. Moreover, there is an event detected only by tomography during July 24th, recognized by the full parameters crosscheck as a possible dust devil.

The first step of the time domain analysis performed only on the pressure parameter has identified a total of 6611 class T events. Such large number of detections shows that a simple pressure phase picker analysis is not sufficient to strictly constrain the identification of dust devils, especially when the noise level is relevant. In order to reduce the number of detected non-significant events and to identify the true possible dust devil, we have selected the events that show a synchronous variation of pressure, wind direction and electric field, analysing using a set of three parameters.

On the other hand, the tomography is specifically calibrated to search for the dust devil signature by analysing one single parameter. The tomogram has reached a good efficiency in the detection, providing a clear classification of the events, allowing to individuate the best candidates. In addition, the tomographic analysis can be performed directly on the raw data, despite the presence of high noise level. As described in Section 2.3, in order to perform the "phase picker" technique on the pressure data, we had to use a running average filter. Instead, no filtering is needed to perform the tomography, because, as discussed in Section 2.2, it is able to eliminate the part of signal that

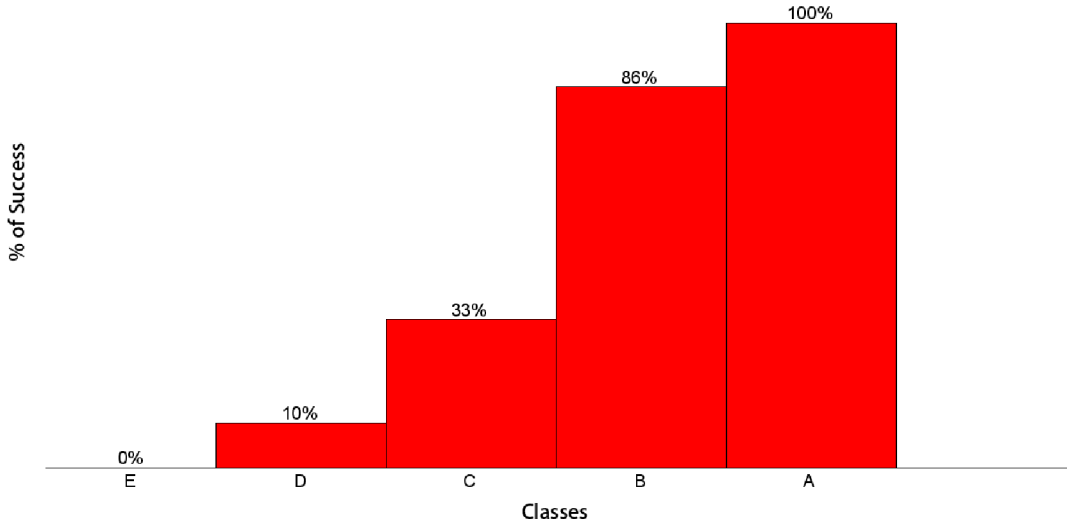

Fig. 9. The percentage of true dust devils, recognized by the full parameters crosscheck, for every class of the tomografic analysis.

Table 4
List of the events identified by the time domain research technique. For each events we report the date, the initial instant (ti), the time duration (Δt), the mean values inside the event of Sensit counts, the maximum wind speed direction change (ΔWdir), the pressure drop (ΔP) magnitude and the class.

ID	Date	ti (h)	Δt(s)	S (counts/s)	ΔWdir (°)	ΔP (mbar)	Classes
P1	17_07_2013	12.115	6.1	0.2	45	0.4	A
P2	17_07_2013	13.0614	9.0	0.0	31	0.3	B
P3	17_07_2013	13.7617	18.7	0.0	175	0.3	A
P4	17_07_2013	15.595	23.0	1.4	31	0.5	A
P5	17_07_2013	17.1817	4.0	2.1	34	0.3	C
P6	17_07_2013	17.8178	4.0	3.1	41	0.3	C
P7	17_07_2013	18.9661	45.0	3.6	94	0.8	A
P8	17_07_2013	20.5736	37.1	0.9	52	0.7	C
P9	17_07_2013	20.6439	36.0	12.8	42	0.7	A
P10	17_07_2013	21.3003	38.9	152.5	60	0.6	C
P11	17_07_2013	21.5617	34.9	35.9	164	1.3	A
P12	17_07_2013	22.0197	12.2	5.3	36	0.3	C
P13	17_07_2013	22.0675	29.9	8.0	51	0.5	B
P14	21_07_2013	12.7928	41.8	0.0	179	0.8	A
P15	21_07_2013	13.3683	13.0	5.9	80	0.5	A
P16	21_07_2013	18.5372	13.0	0.4	37	0.4	C
P17	24_07_2013	9.68722	12.0	0.0	53	0.4	A
P18	24_07_2013	10.9225	24.8	0.1	92	0.7	A
P19	24_07_2013	11.5881	20.9	0.0	94	0.5	A
P20	24_07_2013	16.8775	51.1	0.0	124	0.9	A
P21	10_08_2013	16.7394	41.0	24.4	116	1.0	A
P22	11_08_2013	11.4311	13.0	2.9	120	0.6	A
P23	11_08_2013	13.0119	40.3	0.0	174	0.5	A

does not belong to the dust devil by analysing the coefficient c_θ^i.

4. Conclusions

We have monitored five days of dust devil activity in the Moroccan Sahara tomogram convective vortex pressure core drop detection. This method combines a time operator with a data adapted operator, built from a set of type signals that represent the behaviour of a dust devil pressure signal. The method is automatic and does not require fine-tuning of its parameters.

The algorithm has identified a total of 47 events, classifying them in 5 classes (E, D, C, B and A) from the least probable to the most probable as dust devils. We have crosschecked the events by comparison with the behaviour of the other meteorological parameters, confirming that all the class A events are actually dust devils, while all the class E are not significant detections. The tomography has demonstrated an excellent ability to distinguish between the true dust devils and the false positive events, even analysing only the pressure parameter.

We have tested the efficiency of our method by comparing it with a standard time domain research technique. For this purpose, we have performed a phase picker detection on the pressure measurements, using an eleven second running average to cut the signal noise. In order to eliminate the false positive events, the phase picker algorithm also analyses the wind direction and electric field, looking for the synchronous occurrence of dust devils features in the three parameters. The tomography has given good results compared to the phase picker technique missing only two high probable dust devils and two probable ones, while it has detected a possible dust devil unseen by the other method. In addition, due to its innate ability to filter the background signal components, the tomography does not require the preliminary processing of the pressure data.

The study of dust devils is a topic of great interest in Martian science: these vortices are common and widespread along the planet surface, and they give substantial contribution to the global dust emission, affecting the radioactive budget and the global climate.

However, it is not uncommon that the monitoring of the dust devil's activity by the landed instrument is affected by possible complications. The Viking Meteorology Instrument System on board of the Viking

Table 5
The match between the events identified by time domain research technique and by the tomography technique.

Time domain research				Tomography research			
ID	Date	ti (h)	Class	Match	ID	ti (h)	Class
P2	17_07_2013	13.0614	B	No			
P13	17_07_2013	22.0675	B	No			
P1	17_07_2013	12.115	A	No			
P3	17_07_2013	13.7617	A	No			
P4	17_07_2013	15.595	A	Yes	T11	15.5966	D
P7	17_07_2013	18.9661	A	Yes	T14	18.9736	A
P9	17_07_2013	20.6439	A	Yes	T18	20.6494	B
P11	17_07_2013	21.5617	A	Yes	T19	21.5641	A
P15	21_07_2013	13.3683	A	Yes	T22	13.3691	B
P17	24_07_2013	9.68722	A	Yes	T28	9.6888	B
P18	24_07_2013	10.9225	A	Yes	T29	10.9250	B
P19	24_07_2013	11.5881	A	Yes	T31	11.5891	D
P20	24_07_2013	16.8775	A	Yes	T32	16.8805	B
P22	11_08_2013	11.4311	A	Yes	T44	11.4319	B
P23	11_08_2013	13.0119	A	Yes	T45	13.0125	C
P14	21_07_2013	12.7928	A	Yes	T21	12.8000	A
P21	10_08_2013	16.7394	A	Yes	T38	16.7441	A
	24_07_2013			No	T30	11.0016	D

Lander 1, as well as Meteorology Package on board of the Pathfinder lander and the Rover Environment Monitoring Station on board of the Curiosity rover have expired anomalies with the wind speed and direction detectors, making the wind data totally unavailable in some cases. The lack of these key parameters represents a serious issue for the unambiguous identification of the vortices. The tomography technique could be very helpful in these cases, as it allows the search of dust devils events on the basis of pressure data only, clearly distinguishing between events that are doubtful and highly probable.

In summary, we have shown how the tomography is a reliable method for the dust devils identification and that it has a good detection efficiency. The method provides filtering, separation and characterization of the dust devil signal components even in presence of strong noise. For these reasons, the tomograms could be a useful tool for the detection and characterisation of dust devil events for both terrestrial and Martian campaigns. The algorithm can be modified by using more than one parameter in the analysis. We are working in this direction, and we expect to get more accuracy in the characterization and classification of the dust devils.

Authors contribution

Carlos Aguirre: Mathematical development of the data-driven tomography, software implementation, pressure data processing and data analysis Rui Vilela Mendes: Mathematical development of the tomographic technique in general and the data-driven tomography in particular Luis Vázquez: Data processing and Data Analysis; justification of the results Raquel Caro-Carretero: Data processing and Data Analysis; writing of the paper in general and critical revision of the paper as well as justification of the findings. María Ramírez-Nicolás: writing of the article in general participating actively in the discussion and analysis of the results Gabriele Franzese: development of the time domain detection algorithm, identifying the events with this technique; performance of the crosscheck of the tomography dust devils candidates and execution of the comparison between the tomography and the phase picker results; writing of paper sections relative to these subjects.

Francesca Esposito: took care of the conception, the design, the scientific goals and requirements and the organization of the field campaign; managed the data acquisition. and contributed to the interpretation of the data and to the critical revision of the paper.

Fabio Cozzolino: contributed to the preparation and organization of the field campaign; participated in the data acquisition and Ciprian Ionut Popa: contributed to the organization of the field campaign, providing also help for the selection of the proper site for the dust devil observation; participated in the data acquisition.

Acknowledgements

This work was supported by Ministerio de Economía y Competitividad of Spain (project ESP2016-79135-R) and MINECO DPI 2015-65833-P. We also thank the support of Instituto de Investigaciones Económicas y Sociales Francisco de Vitoria in Spain. This work was also supported by the Italian Space Agency through the agreement I/018/12/0: 'DREAMS EDM Payload—ExoMars 2016'.

References

Aguirre, C., Mendes Vilela, R., 2014. Signal recognition and adapted filtering by non-commutative tomography. IET Signal Proc. 8, 67–75.
Aguirre, C., Serrano, E., Pascual, P., 2013. Detection of neuronal signatures by means of data-driven tomography. BMC Neurosci. 14 (Suppl 1), 309.
Almeida, M.P., Parteli, E.J.R., Andrade, J.S., Herrmann, H.J., 2008. Giant saltation on Mars. Proc. Natl. Acad. Sci. U.S.A. 105, 6222–6226. http://dx.doi.org/10.1073/pnas.0800202105.
Aubry, N., Guyonnet, R., Lima, R., 1991. Spatio-temporal analysis of complex signals: Theory and applications. J. Stat. Phys. 64, 683–739. http://dx.doi.org/10.1007/BF01048312.
Balme, M., Greeley, R., 2006. Dust devils on earth and mars. Rev. Geophys. 44, 3. http://dx.doi.org/10.1029/2005RG000188.
Balme, M., Metzger, S., Towner, M., Ringrose, T., Greeley, R., Iversen, J., 2003. Friction wind speeds in dust devils: A field study. Geophysical research letters 30, 16.
Briolle, F., Man'ko, V.I., Ricaud, B., Vilela Mendes, R., 2012. Non-commutative tomography: a tool for data analysis and signal processing. J. Russ. Laser Res. 33, 103–121.
Crozier, W.D., 1964. The electric field of a New Mexico dust devil. J. Geophys. Res. 69, 5427. http://dx.doi.org/10.1029/JZ069i024p05427.
Crozier, W.D., 1970. Dust devil properties. J. Geophys. Res. 75, 4583–4585. http://dx.doi.org/10.1029/JC075i024p04583.
Daubechies, I., 1990. The wavelet transform: time–frequency localization and signal analysis. IEEE Trans. Inf. Theory 36 (5), 961–1005. http://dx.doi.org/10.1109/18.57199.
Dente, J.A., Vilela, Mendes R., Lambert, A., Lima, R., 1996. The bi-orthogonal decomposition in image processing: Signal analysis and texture segmentation. Signal Process. Image Commun. 8, 131–148.
Donoho, D.L., Stark, P.B., 1989. Uncertainty Principles and Signal Recovery. SIAM. J. Appl. Math. 49 (3), 906–931. http://dx.doi.org/10.1137/0149053.
Duff, N., Lacks, D.J., 2008. Particle dynamics simulations of triboelectric charging in granular insulator systems. J. Electrostat. 66, 51–57. http://dx.doi.org/10.1016/j.elstat.2007.08.005.
Eden, H.F., Vonnegut, B., 1973. Electrical breakdown caused by dust motion in low pressure atmospheres: Considerations for Mars. Nature 280, 962–963. http://dx.doi.org/10.1126/science.180.4089.962.
Ellehoj, M.D., Gunnlaugsson, H.P., Taylor, P.A., Kahanpää, H., Bean, K.M., Cantor, B.A., Gheynani, B.T., Drube, L., Fisher, D., Harri, A.M., Holstein-Rathlou, C., Lemmon, M. T., Madsen, M.B., Malin, M.C., Polkko, J., Smith, P.H., Tamppari, L.K., Weng, W., Whiteway, J., 2010. Convective vortices and dust devils at the Phoenix Mars mission landing site. J. Geophys. Res. 115, E00E16. doi:10.1029/2009JE003413.
Esposito, F., Molinaro, R., Popa, C.I., Molfese, C., Cozzolino, F., Marty, L., Taj-Eddine, K., Di Achille, G., Franzese, G., Silvestro, S., Ori, G.G., 2016. The role of atmospheric electric field in the dust lifting process. GRL 43, 5501–5508. http://dx.doi.org/10.1002/2016GL068463.
Esposito, F., Debei, S., Bettanini, C., Molfese, C., Arruego Rodriguez, I., Colombatti, G., Harri, A.-M., Montmessin, F., Wilson, C., Aboudan, A., Abbaki, S., Apestigue, V., Bellucci, G., Bethelier, J.-J., Brucato, J.R., Calcutt, S.B., Cortecchia, F., Cucciarrè, Di Achille, G., Ferri, F., Forget, F., Friso, E., Genzer, M., Gilbert, P., Haukka, H., Jiménez, J.J., Jiménez, S., Josset, J.-L., Karatekin, O., Landis, G., Lorenz, R., Manetta, M., Martinez, J., Marty, L., Mennella, V., Möhlmann, D., Moirin, D., Molinaro, R., Palomba, E., Patel, M., Pommereau, J.-P., Popa, C.I., Rafkin, S., Rannou, P., Renno, N.O., Schipani, P., Schmidt, W., Segato, E., Silvestro, S., Simoes, F., Simoncini, E., Spiga, A., Valero, F., Vázquez, L., Vivat, F., Witasse, O., Mugnuolo, R., Pirrotta, S., Marchetti, E., 2017. The DREAMS experiment on board the Schiaparelli Module of the ExoMars 2016 mission: design, performances and expected results. Space Rev., under review.
Farrell, W.M., Smith, P.H., Delory, G.T., Hillard, G.B., Marshall, J.R., Catling, D., Hecht, M., Tratt, D.M., Renno, N., Desch, M.D., Cummer, S.A., Houser, J.G., Johnson, B., 2004. Electric and magnetic signatures of dust devils from the 2000–2001 MATADOR desert test. J. Geophys. Res. 109 (E3). http://dx.doi.org/10.1029/2003JE002088.
Fenton, L., Reiss, D., Lemmon, M., Marticorena, B., Lewis, S., Cantor, B., 2016. Orbital Observations of Dust Lofted by Daytime Convective Turbulence. Space Sci. Rev. 203, 89–142.
Fourier, J.B.J., 1888. Théorie analytique de la Chaleur. In: Darbous, G. (Ed.): Oeuvres de Fourier, (Gauthiers-Villars, Paris), Tome premie.
Franzese G., Esposito F., Lorenz R., Silvestro S., Popa C., Molinaro R., Cozzolino F., Molfese C., Marty L., Deniskina N., 2017. Electric properties of dust devils, Earth

Planet Sci. Lett., under review.
Freier, G.D., 1960. The electric field of a large dust devil. J. Geophys. Res. 65 (10), 3504. http://dx.doi.org/10.1029/JZ065i010p03504.
Gimenez-Bravo A., Aguirre C., Vázquez, L., 2013. Tomographic Signal Analysis for the Detection of Dust-Devils in Mars Atmosphere, The Fourth Moscow Solar System Symposium (4M-S3) IKI RAS, 14-18 October.
Greeley, R., 2002. Saltation impact as a means for raising dust on Mars. Planet. Space Sci. 50 (2), 151–155.
Greeley, R., Balme, M.R., Iversen, J.D., Metzger, S., Mickelson, R., Phoreman, J., White, B., 2003. Martian dust devils: Laboratory simulations of particle threshold. J. Geophys. Res. Planets 108 (E5).
Harrison, R.G., Barth, E., Esposito, F., Merrison, J., Montmessin, F., Aplin, K.L., Borlina, C., Berthelier, J.J., Déprez, G., Farrell, W.M., Houghton, I.M.P., Renno, N.O., Nicoll, K.A., Tripathi, S.N., Zimmerman, M., 2016. Applications of electrified dust and dust devil electrodynamics to martian atmospheric electricity. Space Sci. Rev. http://dx.doi.org/10.1007/s11214-016-0241-8.
Husimi, K., 1940.. Some formal properties of the density matrix. Proc. Phys. Mat. Soc. Jpn. 22, 264–314.
Inculet, I.I., Peter Castle, G.S., Aartsen, G., 2006. Generation of bipolar electric fields during industrial handling of powders. Chem. Eng. Sci. 61, 7. http://dx.doi.org/10.1016/j.ces.2005.05.005.
Iversen, J.D., White, B.R., 1982. Saltation threshold on Earth, Mars and Venus. Sedimentology 29, 111–119. http://dx.doi.org/10.1111/j.1365-3091.1982.tb01713.x.
Jackson, B., Lorenz, R., 2015. A multiyear dust devil vortex survey using an automated search of pressure time series. J. Geophys. Res. Planets. 120 (3), 401–412. http://dx.doi.org/10.1002/2014JE004712.
Kano, Y., 1965. A new phase-space distribution function in the statistical theory of the electromagnetic field. J. Math. Phys. 6, 1913–1915.
Klose, M., Jemmett-Smith, B.C., Kahanpää, H., Kahre, M., Knippertz, P., Lemmon, M.T., Lewis, S.R., Lorenz, R.D., Neakrase, L.D.V., Newman, C., Patel, M.R., Reiss, D., 2016. Dust devil sediment transport: From lab to field to global impact. Space Sci. Rev. 203, 377–426.
Kok, J.F., 2010. Difference in the Wind Speeds Required for Initiation versus Continuation of Sand Transport on Mars: Implications for Dunes and Dust Storms. Phys. Rev. Lett. 104, 074502. http://dx.doi.org/10.1103/PhysRevLett. 104.074502).
Kok, J.F., Renno, N.O., 2009. A comprehensive numerical model of steady-state saltation (COMSALT). J. Geophys. Res 114, D17204. http://dx.doi.org/10.1029/2009JD011702.
Lorenz, R.D., 2016. Heuristic estimation of dust devil vortex parameters and trajectories from single-station meteorological observations: Application to InSight at Mars. Icarus 271, 326–337.
Lorenz, R.D., Jackson, B.K., 2016. Dust devil populations and statistics. Space Sci. Rev. 203 (1–4), 277–297.
Man'ko, M.A., Man'ko, V.I., Vilela, Mendes R., 2001. Tomograms and other transforms: a unified view. J. Physics A: Math. Gen. 34, 8321.
Man'ko, V.I., Vilela Mendes, R., 1999. Noncommutative time–frequency tomography'. Phys. Lett. A 263, 53–59.
Murphy, J., Steakley, K., Balme, M., Deprez, G., Esposito, F., Kahanpää, H., Lemmon, M., Lorenz, R., Murdoch, N., Neakrase, L., Patel, M., Whelley, P., 2016. Field measurements of terrestrial and martian dust devils. Space Sci. Rev. http://dx.doi.org/10.1007/s11214-016-0283-y.
Neakrase, L.D.V., Balme, M.R., Esposito, F., Kelling, T., Klose, M., Kok, J.F., Marticorena, B., Merrison, J., Patel, M., Wurm, G., 2016. Particle Lifting Processes in Dust Devils. Space Sci. Rev. http://dx.doi.org/10.1007/s11214-016-0296-6.
Neakrase, L.D., Greeley, R., 2010a. Dust devil sediment flux on Earth and Mars: Laboratory simulations. Icarus 206 (1), 306–318.
Neakrase, L.D., Greeley, R., 2010b. Dust devils in the laboratory: effect of surface roughness on vortex dynamics. J. Geophys. Res.: Planets 115 (E5).
Neubauer, F.M., 1966. Thermal convection in the Martian atmosphere. J. Geophys. Res. 71, 2419–2426. http://dx.doi.org/10.1029/JZ071i010p02419.
Pollack, J.B., Colburn, D.S., Flasar, F.M., Kahn, R., Carlston, C.E., Pidek, D., 1979. Properties and effects of dust particles suspended in the Martian atmosphere. J. Geophys. Res.: Solid Earth 84 (B6), 2929–2945.
Ringrose, T.J., Towner, M.C., Zarnecki, J.C., 2003. Convective vortices on Mars: are-analysis of Viking Lander 2 meteorological data, sols 1–60. Icarus 163 (1), 78–87. http://dx.doi.org/10.1016/S0019-1035(03)00073-3.
Thomas, P.C., Gierasch, P.J., 1985. Dust devils on Mars. Science 230, 175–177. http://dx.doi.org/10.1126/science.230.4722.175.
Wigner, E., 1932. On the quantum correction for thermodynamic equilibrium. Phys. Rev. 40, 749–759.